Colloid Polym Sci 273:719–732 (1995)

ORIGINAL CONTRIBUTION

C.J.G. Plummer
H.-H. Kausch

Real-time image analysis and numerical simulation of isothermal spherulite nucleation and growth in polyoxymethylene

Received: 3 November 1994
Accepted: 14 February 1995

Dr. C.J.G. Plummer (✉) · H.-H. Kausch
Ecole Polytechnique Fédérale de Lausanne
1015 Lausanne, Switzerland

Absract A method of analysing nucleation and crystallization kinetics, based on real time image analysis and hot stage optical microscopy, has been used to investigate the isothermal crystallization of different grades polyoxymethylene. The data were compared with results from differential scanning calorimetry (DSC), using a simple numerical simulation to model the effects of finite sample thickness on the form of the isothermal DSC curves. This simulation was then used to predict the microstructural development in a bulk sample for different boundary conditions, taking into account latent heat evolution and diffusion during crystallization.

Key words Polyoxymethylene – crystallization – image analysis

Introduction

Previous investigations of non-commercial ex-reactor grades of polyoxymethylene (POM) [1–3] have suggested that heat flow rates during both isothermal and non-isothermal crystallization in a differential scanning calorimeter (DSC) can be interpreted successfully in terms of a simplified two-dimensional Avrami model [4]. For the planar 3 mg samples used in these studies the assumptions of rapid heterogeneous nucleation, and of spherulite diameters much greater than the sample thickness, are believed to be justified (as a consequence of the relatively low nucleation density). However, in trying to extend this approach to the isothermal crystallization of as-received commercial POM samples, we have found the nucleation density to be significantly higher, and it is no longer clear that the assumption of two-dimensional spherulite growth can be justified for practical sample thicknesses. Moreover, if one increases the sample size to the point where the geometric criteria for three-dimensional growth are satisfied (that is, that where truncation effects are negligible), thermal inertial and the heat liberated by the growing spherulites may lead to significant temperature differences between the sample holder and the furnace for all but the slowest of crystallizations [3].

Another problem is that even if the assumption of heterogeneous nucleation remains valid, as the density of nuclei increases, the overall crystallization time decreases, and the assumption that the nucleation process occurs over much shorter timescales than the former becomes questionable. Therefore, one may need to include a nucleation rate in the Avrami expression in order to model the crystallization kinetics accurately. In principle, and for a known and constant spherulite growth rate, G, one can obtain the nucleation rate by analyzing the curvature of the spherulite boundaries in a fully crystallized sample [5–8]. This is nevertheless a somewhat lengthy procedure and relies upon the spherulite boundaries being clearly identifiable, which is not necessarily the case in POM samples above a certain thickness. Alternatively, one might attempt to use some assumed analytical expression to fit the DSC heat flow rate curves. However, notwithstanding the problems with sample geometry and size discussed above, the zero time and the initial shape of the heat flow rate curve become difficult to establish unambiguously for fast crystallizations. Furthermore, in isothermal tests, it is not always clear that nucleation itself has

Colloid & Polymer Science, Vol. 273, No. 8 (1995)

occurred isothermally, since cooling from the melt to the final crystallization temperature is inevitably done at a finite rate.

We have therefore chosen to observe the nucleation process directly by hot-stage light microscopy. While this is facilitated by use of a television camera and video recorder, obtaining sufficient data to model the nucleation process as a function of temperature is likely to be time-consuming if each frame has either to be analyzed by hand or downloaded individually to a computer. Fortunately, however, the rapid progress in desktop computer hard- and software has put very powerful image acquisition and analysis techniques at the disposal of the non-specialist, rendering quantitative hot-stage microscopy a more attractive proposition. The same desktop computers may also be used to simulate the spherulite growth processes. Such simulations, based on those described in the literature [3, 5, 6, 8–11], are used here to relate the essentially two-dimensional optical data to the DSC behavior.

As stated above, it may be impractical to measure three-dimensional crystallization rates, depending on the spherulite size. However, if a correlation can be established between the DSC behavior and sample thickness for intermediate cases based on the optical data and computer simulation, this would provide a basis for extrapolating to bulk (three-dimensional) samples, which are clearly of most practical interest. For the same reasons as may invalidate attempts to measure three-dimensional crystallization of POM in the DSC, such extrapolations are in themselves unlikely to provide a very realistic description of bulk crystallization. Nevertheless, given a suitable analytical form for the nucleation rate and spherulite growth rate as a function of temperature it should be possible to simulate what does happen in a bulk sample, taking into account, for example, heat diffusion out of the mold and heat generated by the growing spherulites. This possibility is explored briefly in the final part of the report.

A summary of the basis investigational approach is given in Fig. 1. Several types of POM were initially investigated, including the non-commercial "fluff" grades described in refs. [1–3]. In establishing the link between the optical and DSC data, and bulk microstructures, we have chosen to concentrate on unfilled homopolymers.

Fig. 1 Schematic of the investigational approach

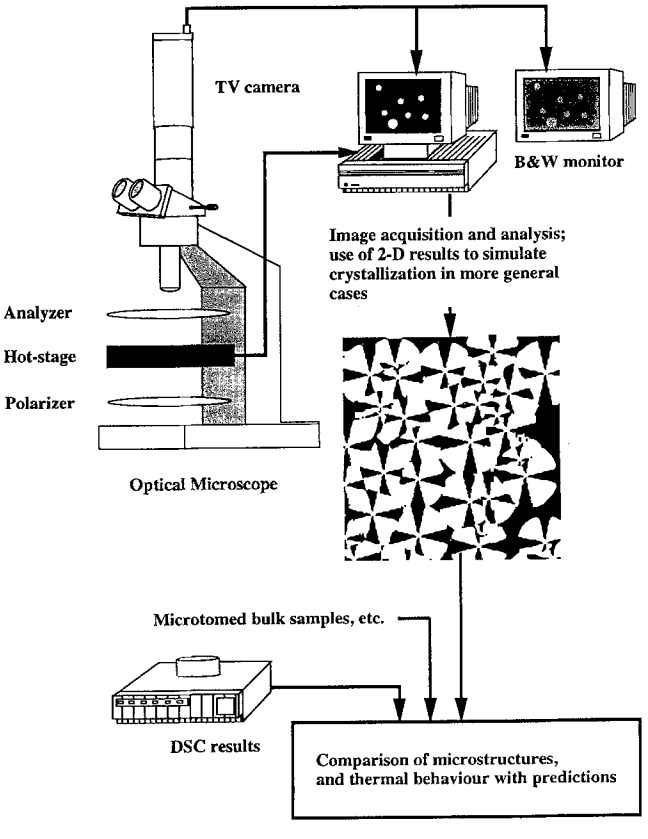

Experimental

The materials were as follows: non-commercial pure POM "fluff" with M_n of 35 000 and 66 000 $gmol^{-1}$ [1–3]; Delrin extruded pellets, again with M_n of 35 000 and 66 000 $gmol^{-1}$ (DuPont de Nemours Ltd). In order to illustrate the optical techniques, results are also given for the POM-based copolymer Hostaform C13021 Nat (Hoechst Celanese – the designation is that of the supplier and M_w is approximately 100 000 $gmol^{-1}$ [12]). The polydispersity of the POM homopolymers was 2.2–2.5, whereas that of the Hostaform copolymer was estimated to be between 4 and 6, with a bimodal molecular weight distribution [12].

The samples were prepared in the form of films pressed at 200 °C between steel plates for a few seconds, and from which circles of diameter 5 mm were cut using a paper punch. The thickness of each sample was determined from its weight, assuming a melt density of 1250 kgm^{-3}. In the case of the optical measurements, the film thickness was kept at or below approximately 70 μm, because of concerns over temperature gradients and the thermal inertia of the samples, which may result in substantial deviations from the temperature displayed by the controller. To check that the temperature remained stable during a given measurement, G was monitored throughout; any variation in G with time was assumed to reflect non-isothermal conditions.

Optical hot-stage microscopy was carried out using the Olympus BH-2 optical microscope equipped with

a Linkham hot stage driven by the Linkham TC 91 temperature controller. The samples were placed between two glass cover slips and viewed between crossed-polarizers under nitrogen gas. To avoid excessive temperature gradients in the samples, the gas was introduced prior to each measurement, and the hot stage was then sealed. Images of the growing spherulites were digitized and analyzed using a Sony DXC 151P color video camera and a Macintosh IIfx computer equipped with the Neotech Image Grabber NBus (the software will be described in the following section). Unless stated otherwise, a fresh sample was used for each measurement, and each sample was melted for 1 min at 185 °C prior to cooling at 75 $Kmin^{-1}$ to the desired crystallization temperature. For a given crystallization temperature, and for both different samples of the same geometry, and repeated measurements on the same sample, these conditions gave results which were reproducible and independent of the prior thermal history. In other words, we were unable to detect significant changes in nucleation density or growth rates as a function of temperature after melting, regardless of the temperature at which the sample had initially crystallized. This was also true of longer melting times (melting times much less than 1 min were of course ruled out by the need to establish thermal equilibrium in the sample) and higher melting temperatures, even though 185 °C is less than the thermodynamic melting point of 200 °C often quoted for POM [13], from which one might infer than autonucleation is an important factor. The reason we preferred to limit the maximum temperature and melting time to 185 °C and 1 min respectively, was to keep sample degradation to a minimum, and the melt viscosity as high as possible (to prevent motion of spherulites during the early stages of crystallization). Note that thermal gravimetric analysis suggested substantial evolution of volatiles to begin after a few minutes under nitrogen at 210 °C in the pure (unstabilized samples). The most immediate effect of this was bubble formation, which invalidated any attempt to interpret the behavior of the sample in terms of its initial geometry.

For DSC measurements the samples were wrapped in aluminum foil to prevent their changing shape during melting, and this also allowed us to put more than one sample in the DSC capsule, providing a means of improving the signal to noise ratio where very thin films were investigated. The measurements were carried out using the Perkin Elmer DSC 7 under nitrogen gas, with the block temperature set to 50 °C and calibrated using indium and zinc standards. The observed melting points used for the calibration were obtained by extrapolating onset temperatures measured at different ramp rates to zero ramp rate. As in the optical observations, all samples were melted for 1 min at 185 °C prior to cooling to the desired crystallization temperature at 75 $Kmin^{-1}$. Again, a fresh sample was used for each measurement, and examined optically after crystallization, in order to verify its integrity.

Computation

Image analysis

Real-time image analysis software was written using the National Instruments Labview programming language, incorporating Graftek Image Concept V.i image handling subroutines and additional subroutines written in Pascal. The basic approach is schematized in Fig. 2. For a film of POM with a thickness of 20 μm or more viewed between crossed-polarizers, crystalline regions of the sample showed roughly uniform birefringence and appeared brighter than the amorphous background (at least for the

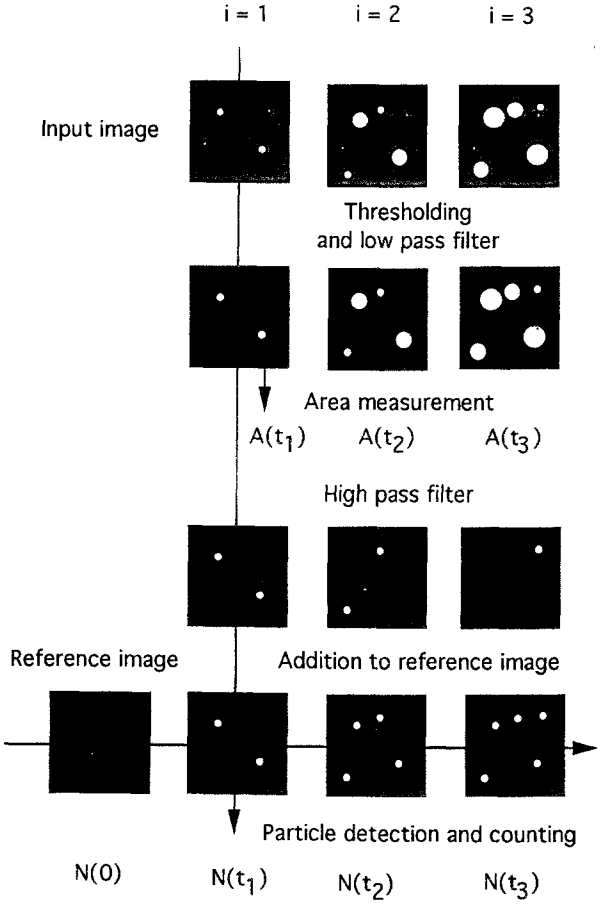

Fig. 2 Schematic of the main loop of the spherulite counting routine: the *i* represent successive iterations (left to right) and the sequence of events during each iteration is shown from top to bottom; once a given image has been added to the reference image, it is discarded in order to free memory for the next input image

crystallization temperatures less than about 160 °C of interest here). Each digitized image of a crystallizing film was converted into a binary image using a suitable threshold intensity, so that all pixels associated with a spherulite took a value of 1, and the background pixels, a value of 0. For the particular binary palette used, the spherulites thus appeared red on black when the image was displayed on the monitor. At this point the total area of the spherulites was measured by counting all the red pixels.

A spatial filter and a particle-detecting routine were used to detect and display spherulites within a chosen size range (4 > area > 1 pixel, for example – the low pass filter was occasionally necessary to eliminate noise in high resolution images). The binary image containing all spherulites meeting the size criterion was then added to a running reference image as shown in Fig. 2 and the total number of spherulites $N(t)$ in the reference image was recorded after each iteration.

The rate at which such data could be acquired depended on the image resolution, particularly since it was necessary to monitor the filtered binary image in order to check for any spurious "spherulites" appearing in the image as a result of noise (for example, from use of an unsuitable threshold for the binary cut). For an image resolution of 96 × 64 pixels images could be analyzed at a maximum rate of about 5 Hz and tests to be described at the end of this section suggested that reliable results for $N(t)$ could be obtained for up to 100 spherulites for a detection size of one pixel (corresponding to an effective area coverage of 1%), as long as neither the nucleation or growth rates were too fast. At higher effective area coverages (lower resolution, higher N_0 or larger detection sizes), underestimates of $N(t)$ owing to overlap of adjacent spherulites were in excess of 2%. For obtaining data at higher acquisition rates, frame-by-frame analysis of a video recording was also available as an option (high resolution and a frequency of 25 Hz combined), but in practice the cooling rate of the hot-stage placed a far more severe limitation than the acquisition frequency on the maximum nucleation rates it was possible to observe. A further problem was that of a transition to a coarser, more heterogeneous internal spherulitic structure as the temperature approached 160 °C, leading to considerable problems in measuring $N(t)$, owing to excessive noise. Nevertheless, the very low nucleation and spherulite growth rates in this temperature range meant that the observer had ample time to count the spherulites appearing on the monitor by hand, if necessary.

In order to interpret $N(t)$ data in terms of a probability of nucleation per unit area of *molten* polymer, spherulite growth must be taken into to account, since clearly a spherulite cannot nucleate in a region already occupied by another spherulite. Thus, if the probability of nucleation of a spherulite in unit area of molten polymer in time dt is given by $p(t)dt$, we have

$$dN(t)/dt = p(t)\left(1 - \frac{A(t)}{A(\infty)}\right) \tag{1}$$

where $A(\infty)$ is the area of the spherulites at infinite time. If we define N_{real} as

$$N_{\text{real}}(t) = \int_0^t p(\xi)d\xi \tag{2}$$

given $N_{\text{real}}(0) = 0$, then since this also implies $N(0)$ and $A(0) = 0$, we can combine Eqs. (1) and (2) and integrate by parts to obtain

$$\begin{aligned} N_{\text{real}}(t) &= \int_0^t \frac{dN(\xi)}{d\xi} \Big/ \left(1 - \frac{A(\xi)}{A(\infty)}\right) d\xi \\ &= \frac{N(t)}{1 - \frac{A(t)}{A(\infty)}} - \int_0^t \frac{N(\xi)}{(1 - \frac{A(\xi)}{A(\infty)})^2} \frac{dA(\xi)}{d\xi} d\xi \end{aligned} \tag{3}$$

The calculation of $N_{\text{real}}(t)$ was performed numerically, using a polynomial fitting procedure to estimate $dA(t)/dt$. Care must be taken for small $dA(t)/dt$ as $A(t)/A(\infty) \to 1$ since the calculated value of $N_{\text{real}}(t)$ becomes very unstable with respect to noise in the image. This also resulted in problems if too high an acquisition rate was used during very slow crystallizations.

The program was initially tested using computer-generated animations of spherulite growth (see the following section) with nucleation occurring with p = constant at each of a finite number, N_0, of randomly distributed sites, such that

$$N_{\text{real}}(t) N_0(1 - \exp(-pt)). \tag{4}$$

Equation (4) also provided a convenient analytical form for the experimental data as will be seen later. As long as $N(t)$ was greater than about 50, and as long as p was less than about one-fifth of the acquisition frequency, the parameters N_0 and p could be well reproduced by fitting of Eq. (4) to the results generated by the image analysis. It was generally necessary to make several measurements in order to find the most judicious choice of experimental conditions (including not only the magnification, image resolution, thresholding and aquisition frequency, but also the sample thickness and the microscope and camera settings). Where doubts persisted in such cases regarding possible noise or insufficient resolution, the results for $N(t)$ were compared with those obtained directly by counting spherulites on video recordings. Otherwise, it was considered sufficient to monitor the filtered binary image, the spherulite count and the original image during the measurement in order to detect and eliminate data containing artefacts. Figure 3 shows typical screen output for

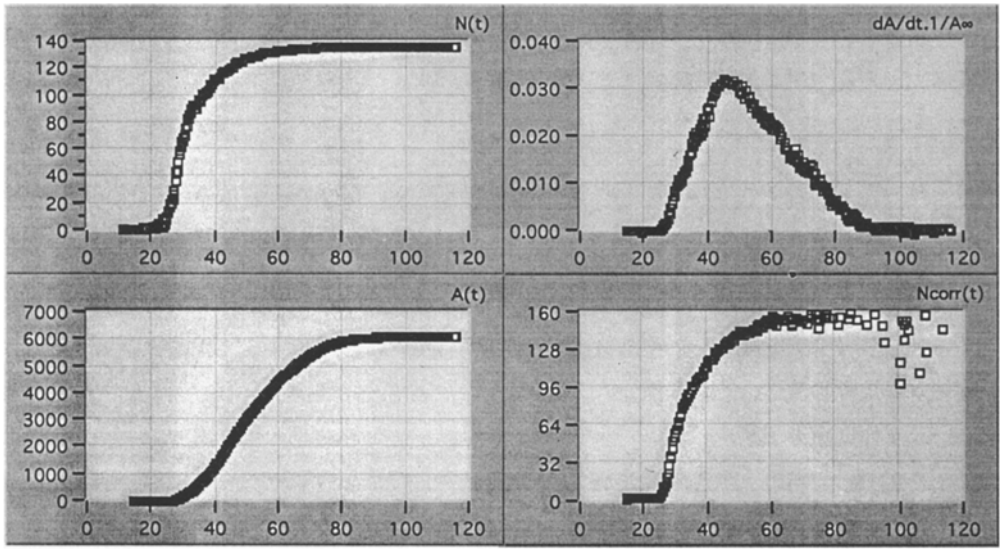

Fig. 3 The screen output generated at 5 Hz for a sample of Delrin $M_n = 66\,000$ gmol^{-1} crystallizing at 151 °C. Note the scatter in $N_{real}(t)$ once crystallization is substantially complete (the horizontal scale is the time in seconds in each case and the total image size was 6144 pixels)

a sample crystallizing at 151 °C and an acquisition rate of ~5 Hz.

Simulation

The basic techniques are introduced here, and discussion of simulations of bulk crystallization follows the Results. Our approach to simulation of spherulite growth was similar to that of other authors [3, 5, 6, 8–11], and needs only be outlined. In two-dimensions, spherulites were nucleated at pseudo-random coordinates within a rectangle according to some chosen nucleation law, and allowed to grow at constant rate (that is, a constant increase in diameter for each iteration). They were drawn as white circles on a black screen and the number of white pixels in some selected sub-region of the box was recorded as a function of the number of iterations (allowing us to avoid edge effects if needed).

In the three-dimensional case, the nuclei were placed within a cuboid box. The fraction of the area of each of 10 equally separated horizontal sections through the box intersected by spherulites was recorded after each iteration, and averaged in order to estimate the extent of volume crystallization (that 10 sections were adequate to give reasonable results for the effective box heights and spherulite densities typically used here, was checked by comparison with simulations using larger numbers of sections; obviously, if the height of the box is very much greater than the mean spherulite diameter, and if the mean spherulite diameter is very much greater than one pixel, one section taken near the center of the box is sufficient). Calculation of the area fraction of spherulites in the two-dimensional sections was treated here as for the case of two-dimensional crystallization, with the following modifications: consider a spherulite which nucleates at some vertical distance d from the plane of a given horizontal section. At the instant t_0 at which the spherulite first intersects the plane, it is as if it has nucleated within that plane at t_0. Thus, the effective nucleation time t_0 is simply the true nucleation time plus d/G (where G is the radial growth rate of the spherulites). The intersection of the (three-dimensional) spherulite with the plane is then a circle, which grows such that at time $t > t_0$ its diameter is given by $(G(t - t_0)^2 + d^2)^{1/2}$ (as opposed to Gt in the two-dimensional case).

For the simulations that follow, a method for obtaining spherulite textures is also required. This may be done using analytical expressions for the form of the spherulite boundaries [5–7]. We initially took this approach, but found it somewhat cumbersome, particularly when included in programs designed to simulate not only the final spherulite structure, but also its evolution. Another option is to use the Macintosh Quickdraw subroutines which manipulate data structures known as regions, each region representing one spherulite in this case. An indication of the form of the spherulite boundaries was obtained by repeated subtraction of the regions, as sketched in Fig. 4. This allowed us to rapidly obtain textures for a large number of spherulites (the maximum number of spherulites to be displayed on the screen was set somewhat arbitrarily to 4000, which was more than adequate). Figure 5 compares typical results with results obtained by calculating the spherulite boundaries analytically. The graphics method gives very ragged boundaries where the growth direction is locally at a very low angle to the spherulite

Colloid & Polymer Science, Vol. 273, No. 8 (1995)

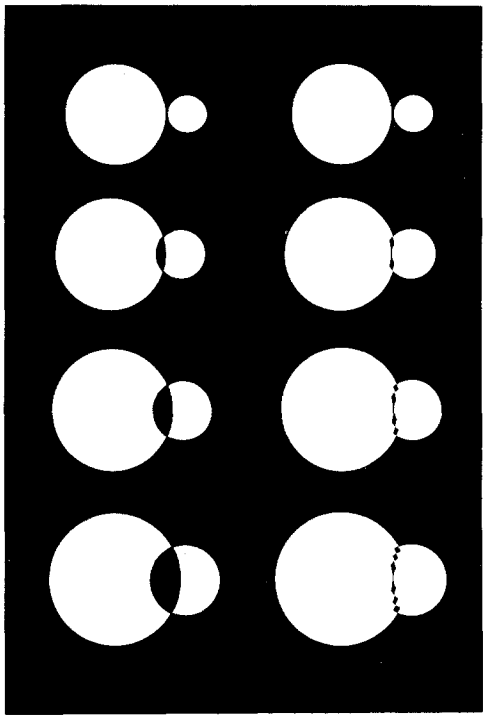

Fig. 4 Generation of spherulite boundaries at each iteration, the intersection of the white circular region representing a given spherulite with all other such regions is subtracted from that region (left-hand column); the result is then superposed onto the regions created during previous iterations (right-hand column)

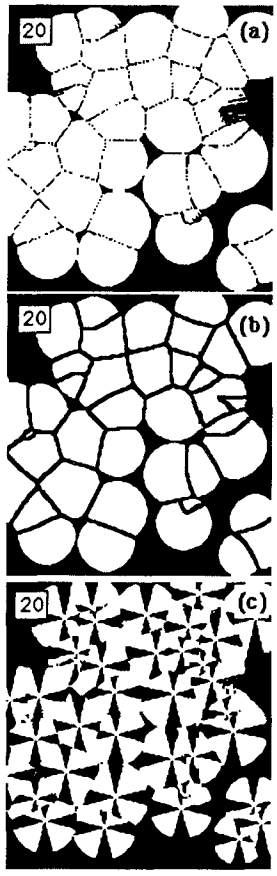

Fig. 5 Comparison of the approach of Fig. 4 (drawing (a)) with an image obtained by calculating the spherulite boundaries from analytical expressions (drawing (b)); drawing (c) is as in (a) but the spherulites have been decorated with "Maltese crosses"; all the drawings are for 40 nucleation sites and 20 iterations, with the spherulite diameters increasing by 2 pixels at each iteration (note that an iterative approach is not needed to obtain drawing (b))

boundary, but otherwise, it suffices to give an overall impression of the microstructure. The shapes of the spherulites can also be highlighted by, for example, painting them in different colors, or as shown in Fig. 5(c) , by superposition of a "Maltese cross" or some other motif.

Results

Nucleation rates

Results for isothermal nucleation rates are given in Fig. 6 for a Delrin POM homopolymer ($M_n = 66\,000\ \mathrm{gmol}^{-1}$) and for the Hoechst Celanese Hostaform copolymer, showing that reasonably good fits can be obtained using Eq. (4) to describe $N_{real}(t)$ vs t. In both cases there were between 60 and 100 spherulites per image and the data represent the superposition of up to three separate crystallizations. There is some independent justification for using Eq. (4) here in that when the samples were subjected to cyclic crystallization, the spherulites tended to reappear in the same positions, although not necessarily in the same order. Thermal nucleation (as opposed to heterogeneous nucleation) appeared very sluggish. It was never possible to observe more than two or three apparently thermally nucleated spherulites (whereas typically samples contained at least 50 heterogeneously nucleated spherulites), and they tended to nucleate late in the crystallization process and thus have little influence on the overall crystallization kinetics. A more thorough investigation of this phenomenon would necessitate use of dispersed droplets, which is beyond the scope of the present report (given sufficient droplets, not containing a heterogeneous nucleation site, one would hope to obtain a reasonable sample of thermal nucleation events).

The probability of nucleation is seen to decrease monotonically with increasing temperature in Fig. 6. One also notes a much lower nucleation rate in Hostaform at a given temperature, consistent with its melting point's generally being some 10 K less than that of the POM homopolymers. In each case the lower limit of the range of crystallization temperatures studied represents the point at which the crystallization rate became too high for it to be possible to achieve nucleation under isothermal conditions at lower temperatures. Instead the spherulites nucleated during cooling from the melt, and the $N(t)$ vs t curves tended to converge as the temperature was lowered further, indicating that the nucleation temper-

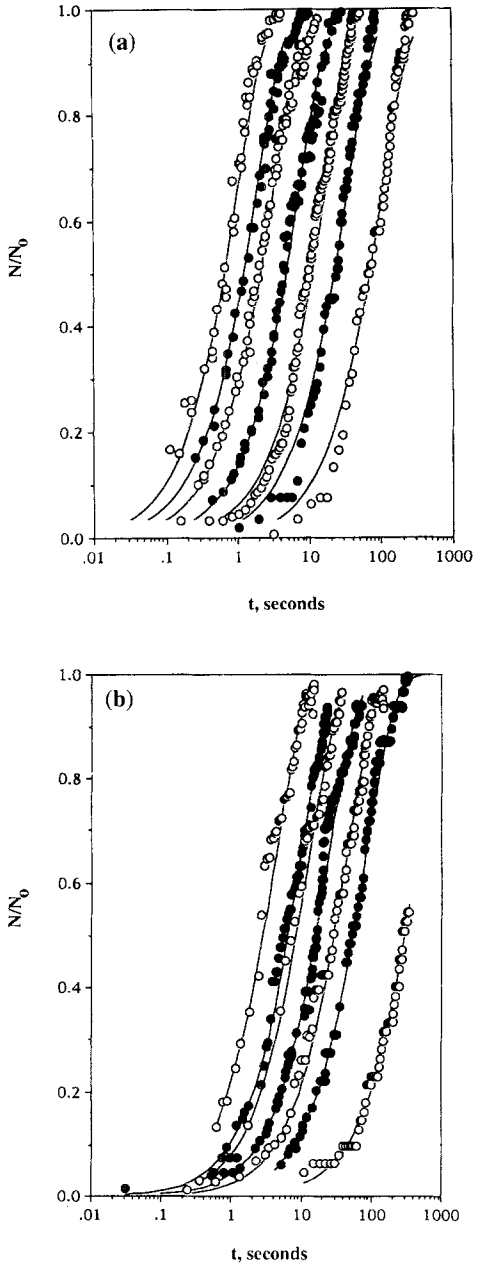

Fig. 6 Fits of $N/N_0 = 1 - \exp(pt)$ to data obtained from (a) Delrin ($M_n = 66000$ gmol^{-1}) between 151° and 157 °C and (b) Hostaform between 147° and 153 °C (T increases in increments on one degree from left to right in both cases)

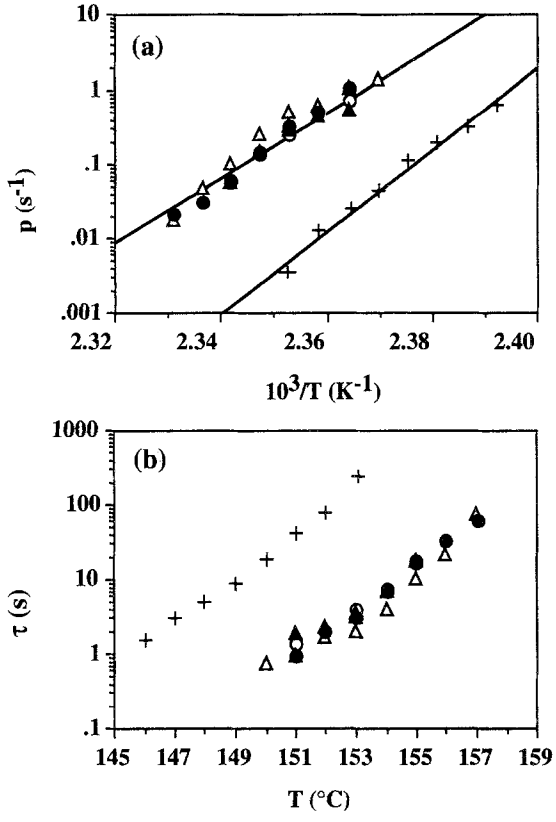

Delrin, M = 66,000 ●; Delrin, M = 35,000 ○; Fluff, M = 66,000 ▲; Fluff, M = 35,000 △; Hostaform C13021 Nat +.

Fig. 7 (a) Nucleation probabilities and (b) characteristic time constants for various grades of POM

ature remained approximately constant regardless of the final crystallization temperature (note that it was not sufficient that the temperature displayed by the temperature controller reach the crystallization temperature by the time the first nuclei are seen, owing to temperature lag between the hot-stage and the sample).

A summary of p values for all the polymers investigated is given in Fig. 7. In Fig. 7(a), $\log(p)$ has been plotted as a function of $1/T$, where T is the crystallization temperature in K, suggested a rough exponential dependence. The results are also plotted in somewhat more accessible form as $\tau = 1/p$ vs T in Fig. 7(b), where τ can be considered to be the characteristic time for the nucleation process. The different molecular weights of fluff and unmodified Delrin polymers showed similar behavior.

The corresponding volume nucleation densities, N_v, have been estimated for different grades in Table 1 from N_0 as obtained from fits to the $N_{corr}(t)$ vs t curves and from the sample thickness. This has been done for a range of thicknesses between about 20 μm and 70 μm, the thickness having been varied in order to check for surface effects, and we find no significant thickness dependence of N_v within the bounds of experimental error. It should nevertheless be noted that the experimental errors are quite large, particularly in the case of Hostaform where the nucleation density was very high, but also for low nucleation densities in very thin films, where the total number of spherulites which could be observed was limited. For the Delrin grades, and in the absence of any influence of the

Table 1 Apparent volume density of nucleation sites, N_v, measured optically

Grade	N_v
Delrin, $M_n = 66\,000$ gmol^{-1}	546 mm^{-3}
Fluff, $M_n = 66\,000$ gmol^{-1}	300 mm^{-3}
Hostaform C13021 Nat	5500 mm^{-3}

film thickness, we estimate an experimental error of about 10%. No significant differences in $p(T)$ were found for the different molecular weights of Delrin investigated. For the fluff grades, the volume nucleation density was about half that in Delrin (see Table 1). For films of 70 μm in thickness corresponding to those used in refs. [1–3] this would give an effective nucleation density per unit area (N_A) of 21 mm^{-2} which compares with the value of 19 mm^{-2} used to fit the data in refs. [1–3].

Overall crystallization rates

By "overall crystallization rates" we refer to the evolution of the proportion of material crystallized, X, as a function of t. In the case of the optical measurements, we define X_{opt} as the fractional area covered by the spherulites in order to distinguish it from X (since the two cannot necessarily be considered equal). Given a known nucleation rate and a known spherulite radial growth rate, G, X_{opt} should be described by the two-dimensional Avrami expression. G is given as a function of temperature in Fig. 8 for various grades as measured directly from video recordings. It was confirmed to be constant as a function of t during crystallizations in the range of T under consideration here. The results were also consistent with those obtained in the past for the fluff grades as indicated in Fig. 8(b), and also those reported by other authors. Also plotted in Fig. 8(b) is the expression

$$\log(G(T)) = 7.7 - 1.96 \times 10^5/T\Delta T - 30\,000/2.3RT\,, \quad (5)$$

where $\Delta T = 473 - T$ (in Kelvin), which we shall consider here as a reasonable empirical description of the data over an extended temperature range (its form in fact arises from theoretical considerations [14]).

A simple derivation of the two-dimensional Avrami equation for instantaneous heterogeneous nucleation was given in ref. [3], and its validity confirmed for sample sizes greater than about 50 spherulites by computer simulation. It would therefore be very surprising if the Avrami approach could not accurately predict $X_{opt}(t)$ in the present case, given reliable data for $N_{real}(t)$, constant G and a sufficient number of spherulites. Indeed, the interest in comparing measured and predicted $X_{opt}(t)$ curves is that it provides a useful check of the consistency of the data.

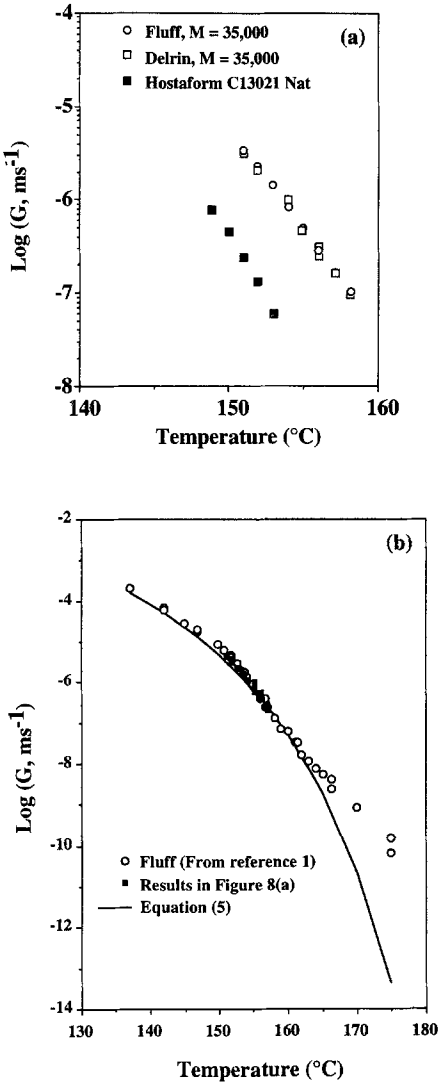

Fig. 8 (a) Spherulite growth rates for various grades; (b) comparison with Eq. (5) and the results given in ref. [1]

Inclusion of a nucleation rate of the form given in Eq. (4) in the Avrami equation leads to

$$\ln(1 - X(t)) = -k\int_0^t (t - \xi)^n \exp(-\xi p)\, d\xi \quad (6)$$

for the general n-dimensional case (in two dimensions $n = 2$ and $k = N_A \pi G^2$, where N_A is the number of nucleation sites per unit area; in three dimensions $n = 3$ and $k = 4/3 N_v \pi G^3$, where N_v is the number of nucleation sites per unit volume) [15]. On integration [15, 16], this becomes

$$1 - X(t) = \exp(-kf(t))\,,$$

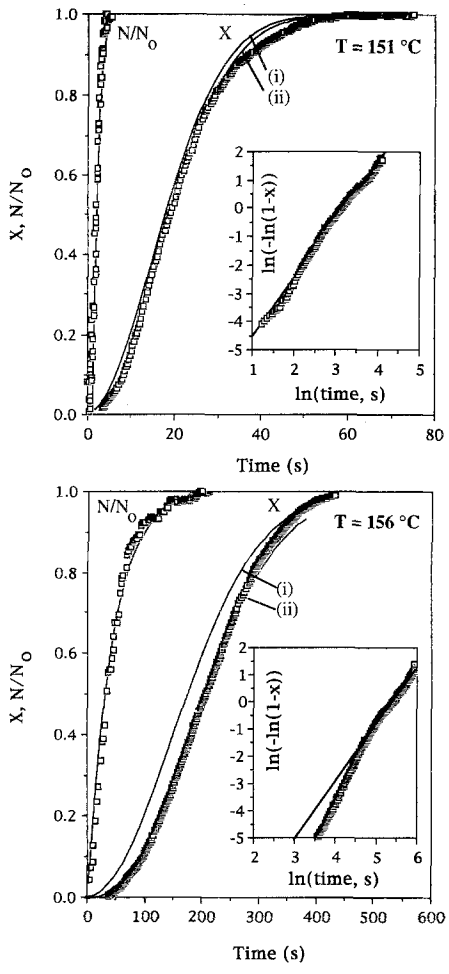

Fig. 9 Comparison of predicted and measured $X(t)$ in optical measurements at two temperatures on Delrin $M_n = 66\,000\ \mathrm{gmol}^{-1}$. Shown are $N_{real}(t)$ and $X(t)$ as a function of time as well as $X(t)$ predicted from Eq. (6) both for (i) instantaneous nucleation and (ii) taking into account the measured p. N_0 was about 64 in both cases (thickness of 70 μm and field of view of 1.66 mm^2)

where in two-dimensions

$$f(t) = t^2 - \frac{2t}{p} - \frac{2}{p^2}(\exp(-tp) - 1)\,.$$

Figure 9 shows a comparison between $X_{opt}(t)$ and the $X(t)$ curves predicted from the measured p, N_A and G data for Delrin, showing good agreement. The deviations at the longest times are due both to the finite number of spherulites and to the presence of voids in the films. It is also found that it made relatively little difference if one assumed instantaneous nucleation in the particular case illustrated, since as one can see from Fig. 9, nucleation remains relatively rapid compared with crystallization in this temperature range. Indeed, an "Avrami" plot of ln(− ln

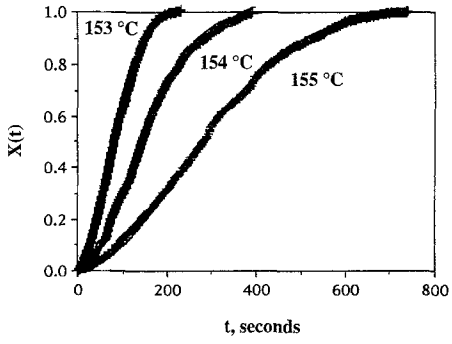

Fig. 10 Predicted and observed $X(t)$ in Delrin, $M_n = 35\,000\ \mathrm{gmol}^{-1}$; the data points are crosses, and these are superposed onto the predicted curves, indicating close agreement

$(1 - X_{opt}(t))$ vs $\ln(t)$ can be fitted to a straight line with slope 2 at 151 °C, as shown in Fig. 9(a). This is not the case at 152 °C (Fig. 9(b)) but this is not to say that the two-dimensional model with instantaneous nucleation does not provide a reasonable first approximation to the real behavior, as can be seen from the curves.

Further examples of predicted and observed $X_{opt}(t)$ using Eq. (6) are shown in Fig. 10 for Delrin $M_n = 35\,000\ \mathrm{gmol}^{-1}$ for a range of temperatures. The samples in Fig. 10 were all approximately 70 μm thick.

Comparison with DSC results

One of the main problems when comparing DSC and optical results is one of calibration, since obtaining exact agreement is clearly dependent on the measurement temperatures being very close in each case. Whereas in principle it should be possible to calibrate the DSC with sufficient precision, that of the hot-stage is limited to about 1 K. To put this in perspective, the growth rate G for example approximately doubles for a change in temperature of 1 K in the regime under consideration here. Hence, it would be somewhat surprising if DSC heat flow rate data could be predicted accurately from the optical data via the computer simulations (indeed, it would be surprising if the DSC results themselves were exactly reproducible). To obtain some idea of the agreement we have used the N_V values quoted in Table 1, but G was adjusted in order to obtain the best possible fit for a given sample thickness using the computer simulations (corresponding p values were obtained by interpolation from Fig. 7). A comparison of the fitted $G(T)$ obtained in this way and the $G(T)$ measured optically is given in Fig. 11 for Delrin, $M_n = 35\,000$, showing that the adjustments to G are relatively minor, and hence that the DSC results are

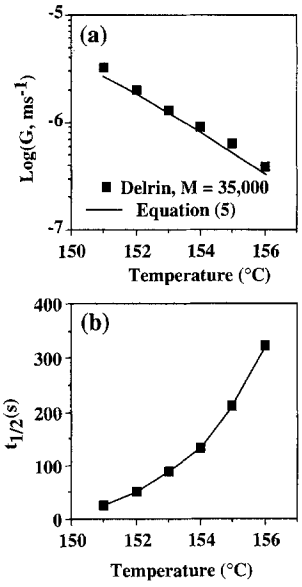

Fig. 11 (a) A comparison of G values observed directly and inferred from DSC crystallization curves in Delrin, $M_n = 35\,000$ gmol^{-1}; (b) crystallization half-times for the same samples as in (a)

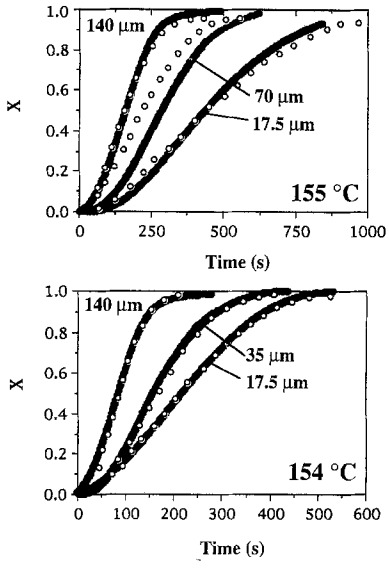

Fig. 12 The effect of sample thickness on DSC crystallization in Delrin, $M_n = 35\,000$ gmol^{-1}; the solid curves are the DSC data and the open circles are the results of computer simulations

at least consistent with the optical data. The crystallization half-times, also given in Fig. 11, are significantly shorter than for the fluff grades [1], again reflecting the lower nucleation density.

Another test is to look at the effect of varying the samples thickness (and hence the geometry and the total number of nucleation sites), for fixed T and hence for fixed G and p. Results are shown in Fig. 12 for Delrin, $M_n = 35\,000$. For relatively low crystallization rates, predictions and observations are broadly consistent up to the maximum sample weights of 6 mg, but we find that for faster crystallization ($T < 153$ °C) the thicker samples cease to behave in accordance with the predictions. This is telling, since we think the reason for the discrepancy is temperature variations in the sample holder over time ranges comparable with the overall crystallization time. This effect is most severe in large samples because of the heat evolved during crystallization; thus a 15 mg sample crystallized at 153 °C will show apparently slower kinetics than a 1 mg sample. We estimate that even for the somewhat lower nucleation densities in the fluff samples that once the crystallization half-time drops below about 30 s, the assumption of isothermal crystallization will begin to be doubtful, which may explain the lower than expected k-values obtained from DSC results for isothermal crystallization in reference 1 for $T < 150$ °C. In samples crystallized at constant cooling rate, and where heat evolution is explicitly accounted for, better agreement is obtained with G values measured independently by hot-stage microscopy [3].

Crystallization in bulk samples

Simulated microstructures

Reference will be made throughout this section to injection moldings, since these are of most interest (industrial applications of POM involve almost exclusively injection moldings). If we ignore flow effects (in fact a serious omission, as will be discussed later), we can consider injection molding simply to involve transfer of a melt at some relatively elevated temperature into a cold mold. Thus the surface layer of the molding will begin to crystallize almost instantaneously. The crystallization front will then advance into the melt interior at a rate essentially determined by the rate of heat diffusion out of the mold cavity. As it does so, heat will be liberated at the solid-liquid interface (the latent heat of crystallization). The effect of this is a gradual flattening off of the temperature profile in the central part of the mold, and so once the temperature in the central part of the mold falls to a certain point, one expects to see the development of an equiaxed microstructure in the remaining molten polymer, as opposed to the directional solidification inward from the melt walls, consistent with observation [17, 18]. On the other hand, if there were no heat evolved by the advancing melt front, one might not expect to see an equiaxed zone, at least in relatively simple geometries.

In the model to be discussed here we take the following simplified approach. We model a two-dimensional section

through an infinite sheet of thickness x_0 and we use a two-dimensional simulation of the microstructural development, assuming G and the nucleation rate to be as for Delrin. N_A is chosen so as to give similar spherulite density to the three-dimensional case ($100\,mm^{-2}$ in the case of Delrin). No attempt is made to take into account heat transfer at the mold walls. The T profile is initially a step function so that at $t = 0$ and for $x < 0$ and $x > x_0$ (x is distance measured across the mold), $T = T_W$, and for $0 \leq x \leq x_0$, $T = T_0$. The principle is then as follows: a layer of nucleated spherulites is placed along each of the mold walls, and some fixed number of potential nucleation sites are scattered at random in the sample interior. A finite difference algorithm is used to calculate the evolution of the T profile, assuming uniform, temperature independent thermal conductivity in the mold interior, and the mold walls to be perfect heat sinks. The surface layers at $x = 0$ and $x = x_0$ are allowed to advance a pixel at a time into the interior of the mold, the time δt taken for each increment being calculated from $G(T(x))$ using expression (5). The total latent heat evolved is converted to a local temperature rise, which is added to the initial T profile corresponding to the newly grown layer. The T profile is then allowed to relax over a time δt and the growth step is then repeated. During each growth step nucleation and growth is allowed to occur ahead of the growth front depending on the local T.

Of course, in general, spherulites growing in a temperature gradient will not evolve as spheres (or as circles in two-dimensions), but as complex shapes determined by their precise temperature environment. However, from comparison of various spherulite growth algorithms, we think this has little influence on the general appearance of the final microstructure, and given that the two-dimensional approximation already leads to an unrealistic spherulite size distribution, more detailed modeling was not considered appropriate. It might also be noted that the latent heat correction was only made at the advancing growth front, and was not applied to spherulites nucleating ahead of the growth front. While this was essentially for pragmatic reasons (it would considerably complicate the calculation of the T profile),

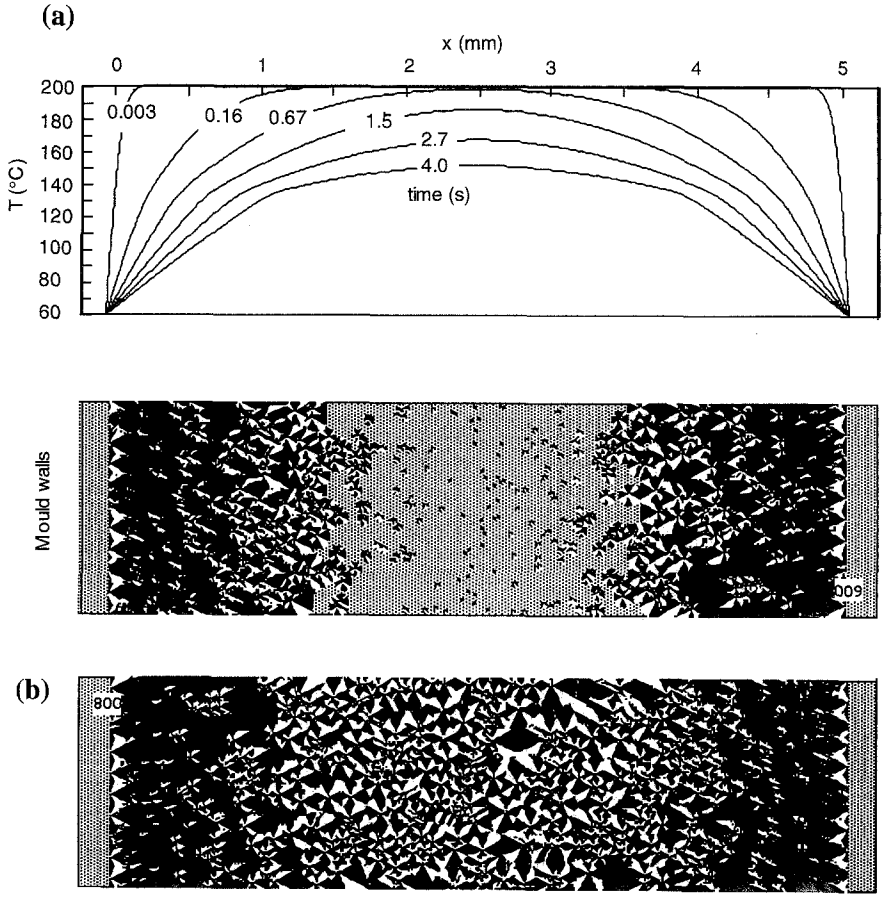

Fig. 13 Simulated microstructure in a 5-mm-thick molding with wall temperature $T_W = 60\,°C$ and melt temperature $T_0 = 200\,°C$: (a) the state of the molding after ~ 5 s, along with selected temperature profiles; (b) the final microstructure

Colloid & Polymer Science, Vol. 273, No. 8 (1995)

as long as the nucleation density is relatively low, the heat liberated by isolated spherulites is likely to have only a minor effect compared to that liberated by the main growth front. This may not be true of the final quasi-isothermal stage of crystallization in the mold center, but should not affect the equiaxed structure. Nevertheless, by not taking this effect into account we are clearly going to underestimate the overall crystallization time.

An example of a simulated microstructure is shown in Fig. 13 for a 5-mm-thick molding and $T_W = 60\,°C$ and $T_0 = 200\,°C$, with an indication of the T profile at different times. Figure 13(a) is the state of the molding after 3.5 s and Fig. 13(b) after completion of crystallization. Note how the T profile at the mold center flattens off with time, and the slight break corresponding to the position of the advancing solidification front, consistent with the results of previous simulations based on the Avrami equation [19]. Further examples of simulated microstructures are given in Fig. 14 for several different T_0 and T_W. While as expected, lowering T_W leads to a wider columnar growth region for a given T_0, the structure appears relatively insensitive to the choice of T_0.

Fig. 14 Microstructure as in Fig. 13, but for various T_W and T_0: (a) $T_W = 120$, $T_0 = 200$; (b) $T_W = 90$, T_0: = 200; (c) $T_W = 60$, T_0: = 200; (d) $T_W = 60$, T_0: = 180

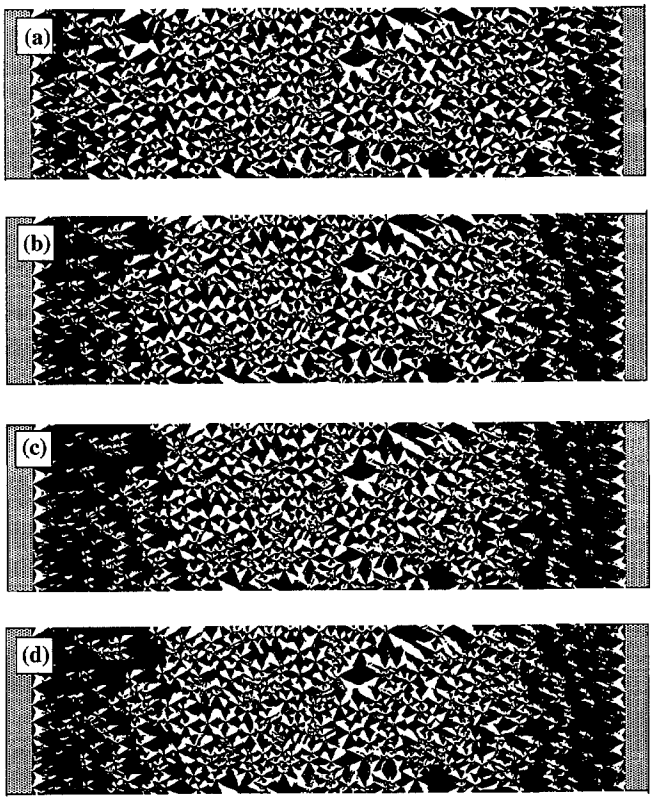

Comparison with observed microstructures

To understand fully the development of structure in POM injection moldings it is necessary to consider not only the interrelationships between thermal history and crystallization kinetics of a quiescent melt, but also the rheological history of the melt and the effect of this on crystallization. The surface layer, or "skin", for example, contains a high degree of molecular orientation and a non-spherulitic microstructure, which Clark suggested to consist of planar lamellae aligned perpendicular both to the surface and to the melt flow direction [17], and to characterize crystallization occurring during the fill time of the mold cycle. Following Clark, subsequent crystallization ought therefore to occur as in the simulations of the previous section, with a layer of columnar growth giving way to an equiaxed region in the center of the molding, and indeed in such cases, the increase in thickness of the columnar zone with decreasing mold temperature appears to be confirmed by observation [17].

Nevertheless, in practice and depending on the molding conditions, the microstructure presented by injection moldings may be considerably more complex than the above simple three-layer scheme, and the melt temperature in particular would appear to play a more decisive role than our simulations suggest [18]. The differences are most apparent in the coarseness of the equiaxed microstructure in the central core region of the samples. Observation of as-received injection moldings of Delrin show that the core structure is often very much finer than could be accounted for by the nucleation densities reported in Table 1, and shows considerable variation both within a given cross-section and along the sample length. This is probably due to mechanical effects, and specifically to shear between a central core in plug-flow and outer, stationary layer as described by Bowman [18]. Figure 15 shows scanning electron microscope (SEM) images of polished sections taken from a typical Delrin injection molding and etched in nitric acid. While the fine structure in the central part of the mold near to the gate generally appears equiaxed (Fig. 15(i)), regions of apparently row-nucleated spherulites (Fig. 15(iii) are frequently observed, which are a clear indication of flow effects. For comparison, Fig. 15(ii) shows the boundary between the skin and the columnar region, showing a relatively unperturbed microstructure. Note the small spherulites which have nucleated just ahead of the solidification front, and then been absorbed by this latter.

Clearly then, mold filling cannot necessarily be considered rapid with respect to the overall cooling time. That the melt temperature may be critical to the microstructure follows from this, since for a given mold temperature, a hot melt will be both less viscous (allowing

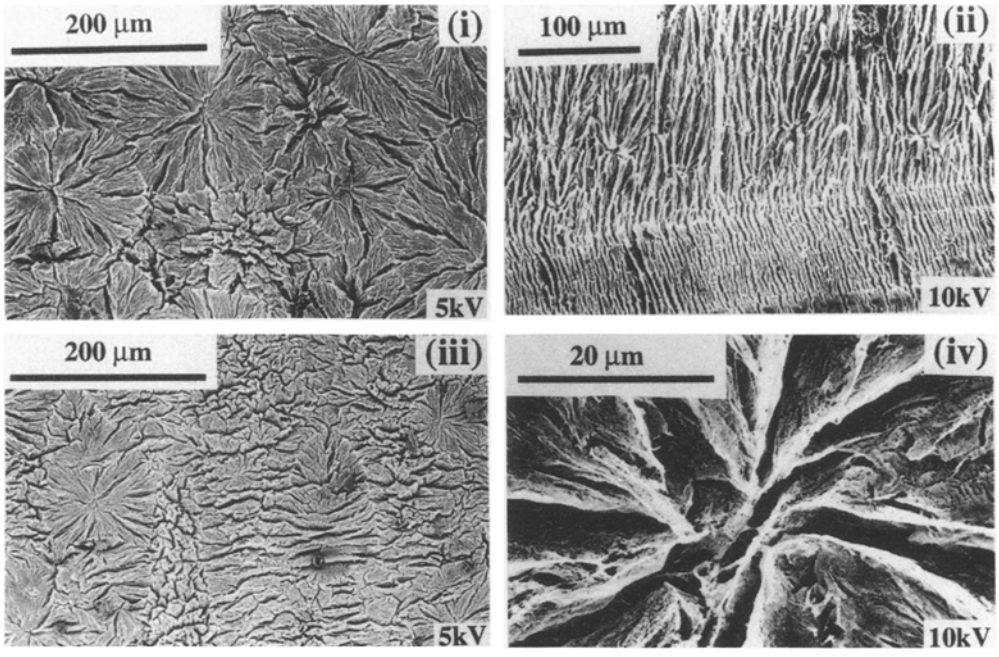

Fig. 15 SEM images of nitric acid etched longitudinal sections through a Delrin $M_n = 66\,000\ gmol^{-1}$ injection molding ($10 \times 5\ mm^2$ rectangular cross-section) : (i) central core region; (ii) boundary between the outer skin and the columnar region; (iii) row nucleation in the central core (flow direction approximately vertical); (iv) detail of (i)

faster relaxation of stress induced orientation), and cool more slowly. Given that we anticipate little variation in nucleation density as a function of the initial temperature of a quiescent melt, observations of somewhat coarser microstructures in injection moldings where the melt temperature is high are probably due to the diminishing influence of flow.

Where flow is important, models not taking into account mechanical effects are most likely to be applicable away from the gate [17], where the melt velocity is relatively low, and the conditions approximate to those of a quiescent melt. In the present case, we have looked at the microstructures of end-gated injection molded bars of Delrin and the fluff grades with two different melt temperatures, taken from the end of the bar furthest from the gate. The microstructure was relatively weakly influenced by the mold temperature and the molecular weight, as anticipated, although it should be remembered that the effective melt temperature may differ from the nominal one owing to effects such as viscous heating. A comparison of the simulated and observed microstructures in Delrin and fluff is shown in Fig. 16. As discussed in the third section, POM spherulites do not show a well-defined Maltese Cross texture, which makes individual spherulites somewhat hard to distinguish in the micrographs. However, the relative widths of the equiaxed core and the columnar regions may be seen to be consistent with those in the simulated microstructures. Under these conditions, the

Fig. 16 Simulation and optical images of microtomed transverse sections taken between crossed polarizers from the ends furthest from the gate of 3-mm-thick injection molded bars of Delrin and fluff with $M_n = 66\,000\ gmol^{-1}$, molded with a melt temperature of 200 °C and a mold temperature of 90 °C: (a) fluff; (b) Delrin; (c) microstructure predicted for fluff; (d) microstructure predicted for Delrin

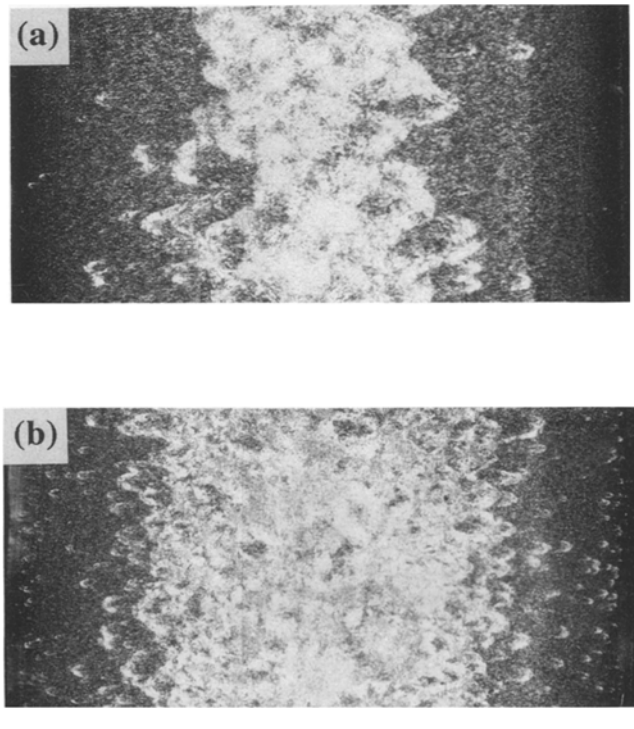

Colloid & Polymer Science, Vol. 273, No. 8 (1995)

simulations suggested the samples to have crystallized in a temperature range of about 130°–140 °C.

Conclusions

An optical method for analysis of nucleation and crystallization kinetics in POM based on real time image analysis has been presented. The results appear to confirm nucleation to be essentially heterogeneous both in commercial grades of POM (Delrin) and in pure fluff grades, with the main difference between the two being the density of potential nucleation sites, which is somewhat higher in Delrin. Nucleation rates and densities, and spherulite growth rates as a function of temperature are then used to simulate the isothermal DSC crystallization kinetics of samples of arbitrary thickness using a simple numerical approach, which avoids the need for the somewhat unrealistic assumptions inherent in the use of the two- and three-dimensional Avrami expressions (it turns out that in Delrin, the nucleation rate does not have a strong influence on the overall crystallization kinetics). Even for samples of a few mg in the DSC, temperature lag and evolution of latent heat during rapid crystallization may cause the assumptions of isothermal crystallization to break down. This is almost certainly the case during rapid bulk crystallization such as occurs in injection molding.

An outstanding question prior to this investigation was that of the temperature at which an injection molding crystallizes, since it is difficult to infer a crystallization temperature directly from the mold and the melt temperature. While we are still not in a position to answer this question precisely, the simulations of the rapid crystallization of a quiescent melt presented here, taking into account heat evolution and diffusion during crystallization, establish lower limits for a given set of boundary conditions (flow effects would presumably accelerate crystallization at a given temperature and thus raise the effective crystallization temperature somewhat). In certain regions of injection moldings or for certain molding conditions, this may be true, and under such conditions observed and simulated microstructures appear to be in reasonable agreement. In general, however, ignoring flow effects is not justified and we think that they are the key to microstructures frequently encountered in POM injection moldings, which are much finer than would be consistent with crystallization of a quiescent melt. This should be qualified by noting that the simulations require extrapolation of growth rates and nucleation rates and densities to lower temperatures than can be investigated under isothermal conditions. However, if this is justified, then we suggest that in the case of POM and contrary to what is often assumed, fine microstructures do not necessarily reflect relatively low crystallization temperatures. Similarly, the suggestion that fine microstructures arising from relatively low melt temperatures (less than the thermodynamic melting point cited by some authors) are a consequence of autonucleation appears unfounded since there is no evidence for autonucleation in the range of temperatures of practical importance for injection molding ($> 180\,^{\circ}C$).

As regards future work, the computer-aided optical technique is promising as a means for investigating nucleation kinetics and as a complementary technique to DSC investigations, and it should be possible to extend it to polymers other than POM. Realistic simulation of the microstructure of injection moldings remains a somewhat daunting task, but with some refinement, the approach taken here may be of more immediate interest for problems in which flow effects are either absent, or relatively easy to characterize, including compression molding between cold plates, and welding.

References

1. Plummer CJG, Kausch H-H (1994) Polymer Bulletin 32:117
2. Plummer CJG, Kausch H-H (1994) J Mat Sci 13:856
3. Plummer CJG, Kausch H-H (1995) Colloid Polym Sci 273:227
4. Avrami MJ, J Chem Phys 7:1103 (1939); 8:202 (1940); 9:177 (1941)
5. Gałęski A (1981) J Poly Sci – Poly Phys Ed 19:721
6. Gałęski A, Piórkowska (1981) J Poly Sci – Poly Phys Ed 19:731
7. Gałęski A, Piórkowska (1983) Colloid Polym Sci 261:1
8. Billion N, Haudin JM (1993) Colloid Polym Sci 271:343
9. Hay JN, Przekop ZJ (1979) J Poly Sci – Poly Phys Ed 17:951
10. Gałęski A, Piórkowska (1983) J Poly Sci – Poly Phys Ed 21:1313
11. Gałęski A, Piórkowska (1983) J Poly Sci – Poly Phys Ed 21:1299
12. Philippoz J-M (1994) Private communication, DuPont, Geneva
13. Polymer Handbook, Brandrup J, Immergut EH (1989) Eds John Wiley, New York
14. Hofmann JD (1983) Polymer 24:3
15. Aggarwal SL, Marker L, Kollar WL, Geroch R (1966) J Polym Sci A2 4:715
16. Ravindranath K, Jog JP (1993) J Appl Poly Sci 49:1395
17. Clark ES (1973) Appl Poly Symp 20:325
18. Bowman J, Harris N, Bevis M (1975) J Mat Sci 10:63
19. Dimian A (1986) PhD Thesis Conservatoire National des Arts et Métiers, Paris